Solid State Sciences 111 (2021) 106449

Contents lists available at ScienceDirect

Solid State Sciences

journal homepage: http://www.elsevier.com/locate/ssscie

# $MnS_2$/carbon nanotube electrode for improved supercapacitor performance

Rahul B. Pujari [a], Abhishek C. Lokhande [b], Abhijeet R. Shelke [c], Shital B. Kale [d], Dong-Weon Lee [a,**], Chandrakant D. Lokhande [d,*]

[a] MEMS and Nanotechnology Laboratory, School of Mechanical System Engineering, Chonnam National University, Gwangju, 61186, Republic of Korea
[b] Department of Physics, Khalifa University of Science and Technology, P.O. Box-127788, Abu Dhabi, United Arab Emirates
[c] Department of Physics, Tamkang University, Tamsui 251, Taipei, Taiwan
[d] Centre for Interdisciplinary Research, D.Y. Patil University, Kolhapur, 416 006, India

ARTICLE INFO

*Keywords:*
Carbon nanotube
Cyclic voltammetry
$MnS_2$
SILAR
Supercapacitor

ABSTRACT

Manganese sulfide is promising material for electrochemical applications. In this work, crystalline, porous, and nanostructured $MnS_2$ and $MnS_2$/carbon nanotube electrodes are prepared using dip dry and successive ionic layer adsorption and reaction (SILAR) methods at room temperature (300 K). Comparative charge storage of $MnS_2$ and $MnS_2$/carbon nanotube is examined in aqueous $Na_2SO_4$ and KOH electrolytes. The superior charge storage of $MnS_2$/CNT in $Na_2SO_4$ is observed with highest specific capacitance of 855 F $g^{-1}$ at 1 mA $cm^{-2}$ current density and 90.1% capacitance retention for continuous 5000 charge discharge cycles. The improvement in electrochemical charge storage of $MnS_2$/CNT is associated with reduced electron transfer path and low equivalent series resistance (ESR) in $Na_2SO_4$.

## 1. Introduction

Supercapacitors are modern energy storage devices with moderate energy density and high power density features useful in wearable electronics, and hybrid electric vehicles [1–5]. Commercially available supercapacitors are assembled using carbon materials electrodes such as graphene, and carbon nanotubes (CNTs) [6–9]. However, their low energy density (<10 Whkg$^{-1}$) is major bottleneck for further development and it can be increased by replacing carbon based electrodes by composites of metal sulfide (rich redox active) and carbon (High surface and high conductivity) materials [10–12]. The composite electrodes prepared with reduced graphene oxide (rGO) and CNTs endow with high specific capacitance and improved energy density owing to increase in electrochemical active sites and increase in electrical conductivity.

Recently, different strategies are employed for preparation of composite and hybrid electrodes such as MnS [13–17], NiS [18–21], CuS [22–25] etc to increase energy density of supercapacitors. The metal sulfide electrodes show higher energy density and power density compared with corresponding metal oxide electrodes owing to higher electrical conductivities, however, low cyclic lifetime is major challenge for them. Cyclic stability of metal sulfide electrodes can be increased by different strategies such as making composite or hybrid electrodes with rGO [26] and CNTs [27–29], or core-shell structures preparation [30] etc. Moreover, finding suitable electrolyte for metal sulfide and composite electrodes is also necessary to guarantee maximum charge storage and that can achieved through systematic electrochemical study of electrode storage in different compatible electrolytes.

Present work comprises preparation of $MnS_2$ by SILAR method at room temperature (330 K) and its application to supercapacitor properties. Moreover, improvement of electrochemical charge storage of $MnS_2$ is achieved through $MnS_2$/CNT preparation and systematic electrochemical study of $MnS_2$ and $MnS_2$/CNT is presented in $Na_2SO_4$ and KOH to decide suitable electrolyte.

## 2. Experimental

Manganese sulfate ($MnSO_4$), and sodium sulfide hydrate ($Na_2S.xH_2O$) were purchased from Sigma Aldrich Ltd Mumbai, India. Carbon nanotubes (CNTs), sulphuric acid ($H_2SO_4$), and nitric acid ($HNO_3$) were purchased from Sigma Aldrich Pvt. ltd. USA. De-ionised (DI) water was used for preparation of chemical solutions.

* Corresponding author.
** Corresponding author.
*E-mail addresses:* mems@jnu.ac.kr (D.-W. Lee), l_chandrakant@yahoo.com (C.D. Lokhande).

https://doi.org/10.1016/j.solidstatesciences.2020.106449
Received 21 April 2020; Received in revised form 15 October 2020; Accepted 16 October 2020
Available online 5 December 2020

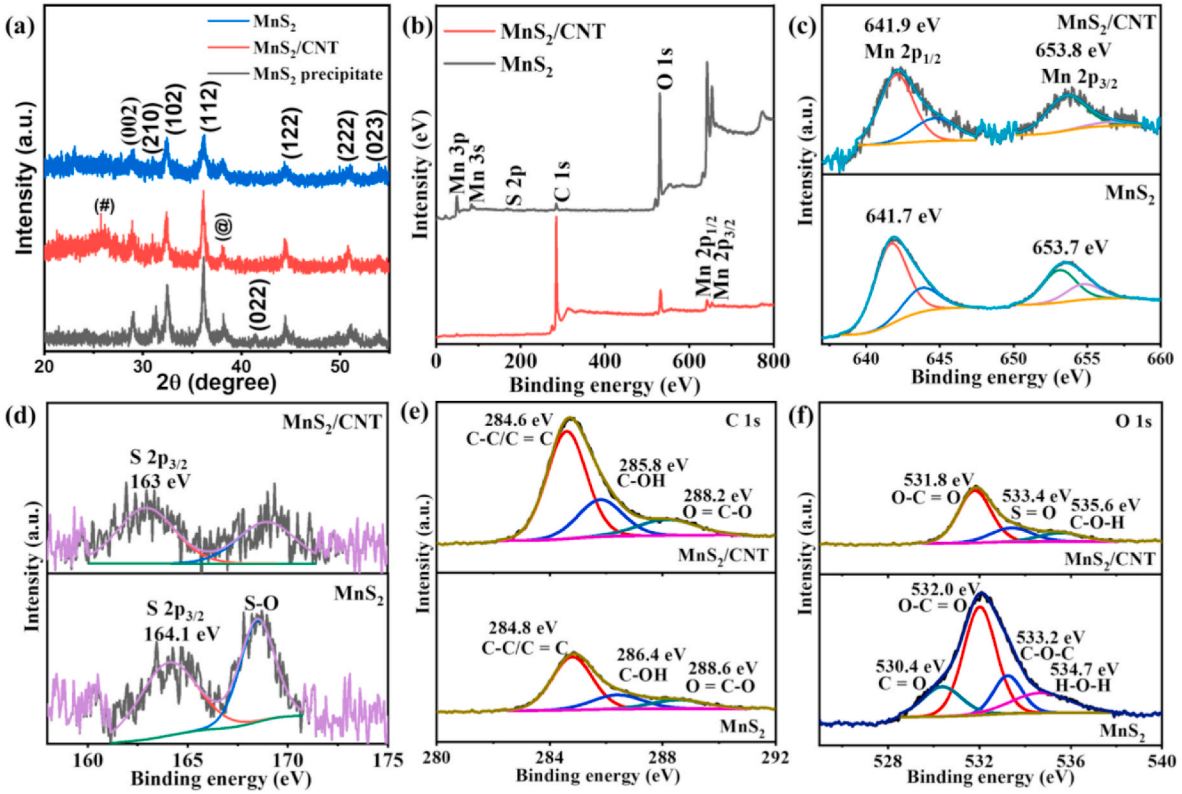


**Fig. 1.** (a) Comparative X-ray diffraction patterns, and (b) survey scan XPS profile of $MnS_2$ and $MnS_2$/CNT thin films. Narrow scan XPS profiles of (c) manganese, (d) sulphur, (e) carbon and (f) oxygen elements in $MnS_2$ and $MnS_2$/CNT thin films.

### 2.1. $MnS_2$ preparation

$MnS_2$ thin film was prepared on 304 type stainless steel (SS) substrate ($1 \times 5$ $cm^2$) using successive ionic layer adsorption and reaction (SILAR) method at room temperature (~300 K). Initially, SS substrate was well-polished with silicon carbide paper and cleaned with ethanol and DI water. Then, it was immersed in 50 ml of manganese sulfate (0.05 M) solution for 20 s (where adsorption of $Mn^{+2}$ ions occur). Then, it was dipped for 40 s in 50 ml of sodium sulfide (0.1 M) solution. There is no drying between adsorption and reaction steps in the preparation of $MnS_2$. Immediately after adsorption of $Mn^{+2}$, SS substrate was immersed in sodium sulfide solution. Thus, single SILAR cycle was completed to form layer of manganese sulfide on SS substrate. The successive 100 SILAR cycles were repeated to form terminal thickness of $MnS_2$ thin film. After each cycle, substrate was rinsed in DI water for 10 s and next cycle was initiated without any delay. Hence, approximately 2 h was required to prepare $MnS_2$ thin film with the mass loading of 0.7 mg $cm^{-2}$.

### 2.2. $MnS_2$/CNT preparation

Dip-dry and SILAR methods were adopted to prepare $MnS_2$/CNT thin film on SS substrate. Initially, 10 mg of activated CNTs (Please see supplementary information for activation of CNTs) were homogeneously dispersed in 50 ml of DI water using Tip sonicator and identified as CNT precursor solution. Then, CNTs were coated on SS substrate by dip-dry method. A dipping time of SS substrate in CNT precursor solution was optimised to 20 s and drying time as 60 s. One dipping and drying cycle of CNTs was followed with SILAR cycle of $MnS_2$ (as identical with the used in section 2.1). After each $MnS_2$/CNT cycle, SS substrate was rinsed in DI water for 10 s. Thus, 160 $MnS_2$/CNT cycles were repeated to load ~0.7 mg $cm^{-2}$ mass of $MnS_2$/CNT thin film on SS substrate. Schematic of $MnS_2$/CNT preparation is presented in Fig. S1. Large area thin films of brown $MnS_2$ and brown-black $MnS_2$/CNT (Fig. S2) were prepared to demonstrate an industrial applicability of present method.

### 2.3. Materials characterizations

Materials were analysed for crystal structure using X-ray diffraction technique (X-ray diffractometer; X'Pert Pro, Malvern Panalytical B.V.) with Cu Kα radiation. Chemical composition and elemental valence states of $MnS_2$ and $MnS_2$/CNT thin films were studied using X-ray photoemission spectroscopy (XPS) technique (ESCALab Mark II, VG Scientific Ltd.) with Al-Kα radiation as the X-ray source. Surface morphology of thin films were examined using field-emission scanning electron microscopy (FE-SEM) (SU-70, Hitachi High Technologies). High resolution transmission electron microscopy (HR-TEM; Philips TECNAI F20) was used to verify nanomaterials, crystal structure, materials. Electrochemical charge storage was evaluated in three electrode setup in 1 M $Na_2SO_4$, and 1 M KOH electrolytes using cyclic voltammetry (CV) and galvanostatic charge discharge (GCD) techniques. Reference and counter electrode were the saturated calomel electrode and platinum plate, respectively. $MnS_2$ and $MnS_2$/CNT thin films were used as working electrodes. Electrochemical impedance were performed in the frequency range of 0.1–$10^5$ Hz using ZIVE MP1 electrochemical work station of Wonatech Company.

## 3. Results and discussions

$MnS_2$/CNT thin film was prepared by combination of dip-dry and SILAR methods. Initially, CNTs were coated on SS substrate by dip-dry method. Then, $MnS_2$ was deposited by heterogeneous chemical precipitation on CNT/SS substrate. $MnS_2$ thin film was formed on SS substrate in anionic (sulphur) precursor by the chemical reaction between $Mn^{+2}$ and $S^{-2}$. In detail, the dissociated $Mn^{+2}$ ions in cationic beaker were adsorbed on SS substrate during the adsorption step and $MnS_2$ layer is

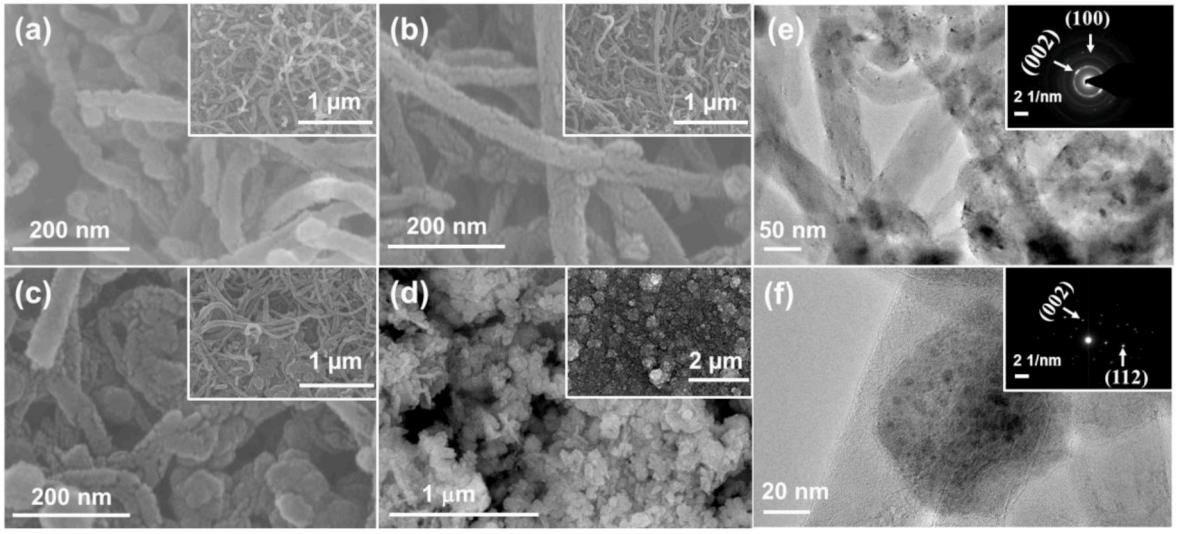


**Fig. 2.** FE-SEM images of (a) pristine and (b) activated CNTs, (c) $MnS_2$/CNT and (d) $MnS_2$ thin films, and (e, f) HR-TEM images of $MnS_2$/CNT. Inset of FE-SEM images (a–d) show low resolution FE-SEM images and inset of HR-TEM images (e, f) show SAED patterns of CNT and $MnS_2$, respectively.

formed in the next step by reaction with sulphur ions ($S^{-2}$) (Fig. S1). The increase in oxidation state of ($Mn^{+4}$) was occurred in the reaction with sulphur ions at 300 K. When SS substrate (carrying $Mn^{+2}$ ions) is dipped in sulphur precursor solution, $S^{-2}$ (in the 0.1 M aqueous $Na_2S$ solution) ions attack very high in number on $Mn^{+2}$ ions on the SS substrate. Thus, high energy system is formed at the SS substrate surface vicinity to $Mn^{+2}$ ions. In order to achieve ground state, manganese (d-block element) reacts with crowded electrophilic sulphur ($S^{-2}$) ions and shift their oxidation state ($Mn^{+2}$) from +2 to +4. Similarly, $MnS_2$ has been prepared elsewhere at the low temperature reactions and oxidation of $Mn^{+2}$ was caused by higher content of sulphur precursor ($Na_2S$ or thioacetamide) [31–33].

$MnS_2$ precipitate sample was prepared for XRD study by collecting formed precipitate in the sulphur precursor solution during the

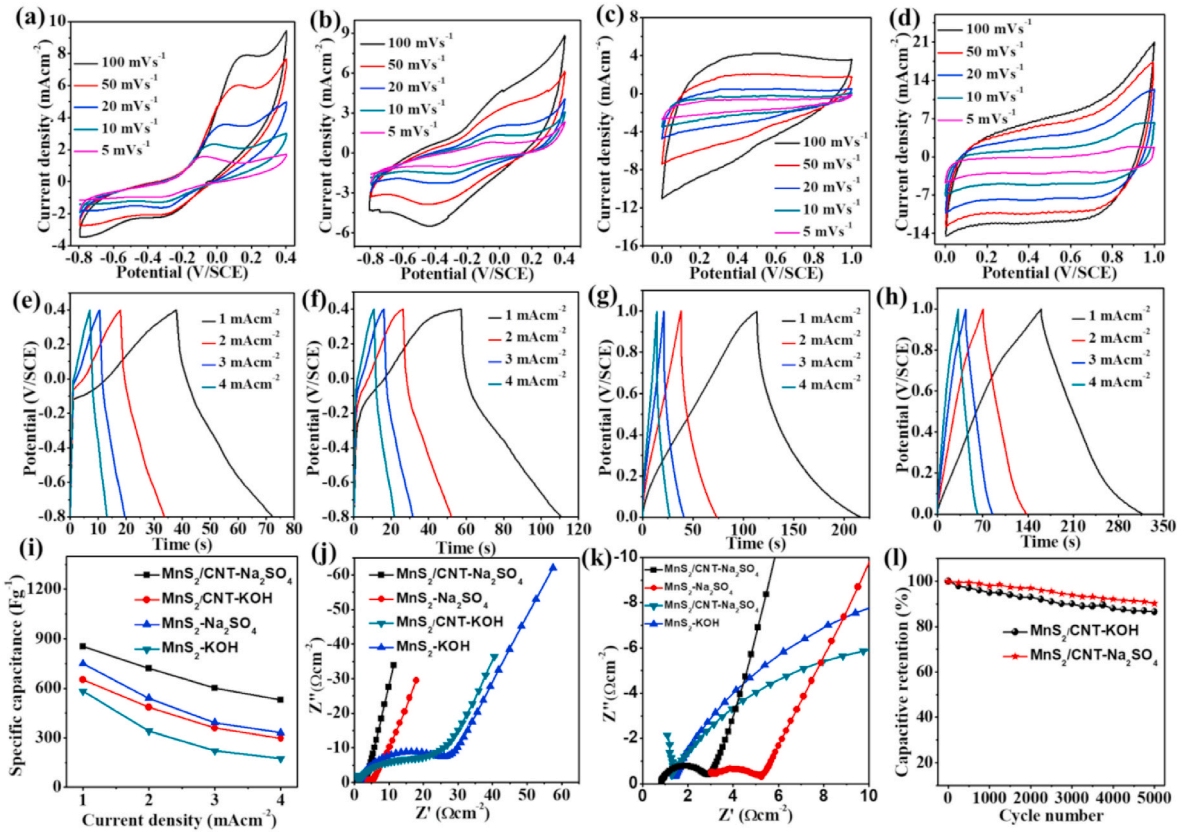


**Fig. 3.** The 5 to 100 $mVs^{-1}$ scan rate CV curves of $MnS_2$ in (a) 1 M KOH and (c) 1 M $Na_2SO_4$, and $MnS_2$/CNT in (b) 1 M KOH and (d) 1 M $Na_2SO_4$. The GCD curves of $MnS_2$ in (e) 1 M KOH and (g) 1 M $Na_2SO_4$, and $MnS_2$/CNT in (f) 1 M KOH and (h) 1 M $Na_2SO_4$. The comparison of (i) Specific capacitances, and (j) impedance spectra of $MnS_2$ and $MnS_2$/CNT in two different electrolytes. (k) Magnified high frequency region of impedance profile. (l) Comparative cyclic stability study of $MnS_2$/CNT for 5000 cycles in two different electrolytes.

preparation of $MnS_2$ thin film. Moreover, another two samples were prepared by scratching $MnS_2$ and $MnS_2$/CNT thin films from SS substrate. Fig. 1 (a) shows XRD patterns of all three different samples, comprising XRD peaks at 2θ positions of 28.9°,31.1°, 32.4°, 36.2°, 41.4°, 44.4°, 50.8°, 53.9° correspond to (002), (210), (102), (112), (022), (122), (222), and (023) planes of cubic $MnS_2$ phase (COD ID: 9008044). In case of $MnS_2$/CNT sample, additional XRD peak (marked with #) is observed at 25.3° corresponds to (002) graphitic plane of CNT and all other peaks are correspond to $MnS_2$ phase of manganese sulfide [34]. A single impurity peak (dictated with @) is observed in all XRD patterns, which corresponds to γ-MnS phase of manganese sulphide. The pristine and activated CNTs show XRD peaks at 25.3° and 42.20° correspond to (002) and (100) planes (Fig. S3) [35]. Broad graphitic peak of (002) plane confirms layered hexagonal crystal structure [36].

The XPS study determines surface chemical composition of $MnS_2$ and $MnS_2$/CNT thin films through Fig. 1(b–f). Survey scan profiles (Fig. 1 (b)) show that Mn and S are present in $MnS_2$ and $MnS_2$/CNT thin films. Mn 2p profile in Fig. 1 (c) is splitted in Mn $2p_{3/2}$ and Mn $2p_{1/2}$ energy doublets, with the 641.7 and 653.7 eV binding energies for $MnS_2$, while 641.9 and 653.8 eV for $MnS_2$/CNT (with 12 eV energy separation for both the samples) supporting for existence of $MnS_2$ phase of manganese sulfide. In our previously published work, it is found that the energy separation of Mn 2p doublet (Mn $2p_{1/2}$ and Mn $2p_{3/2}$) of $MnS_2$ phase of manganese sulfide is highest (12.0 eV) comparison with the γ- and α-MnS (11.6 eV) phases [32]. Thus, it is verified that $MnS_2$ phase of manganese sulfide is formed [32]. S 2p XPS profile shows metal sulfide (Mn–S) bonding in both thin films, which is indicated by S $2p_{3/2}$ peak (Fig. 1 (d)) [37,38]. Owing to air oxygen exposure, both the thin films show S–O bonding in S 2p profile.

The C 1s profile shows C–S bonding at 285.8 eV for $MnS_2$/CNT [39], indicating attachment of S species to CNT during material preparation. The broad scan XPS profile of $MnS_2$/CNT shows low intensity O 1s peak (Fig. 1 (b)) and narrow scan S 2p profile (Fig. 1 (d)) shows decreased ratio of sulfate (related to S–O bonding) to sulfide (related to Mn–S bonding) peaks compared with $MnS_2$. It is concluded that composite ($MnS_2$/CNT thin film) is protected from adsorption of atmosphere oxygen. Because, carbon nanotubes do not form a bond with oxygen at ambient condition, even though exposed to atmospheric oxygen and many $MnS_2$ nanoparticles on the $MnS_2$/CNT thin film are grown below CNT matrix, which is evidenced from FE-SEM results, Such, $MnS_2$ nanoparticles are hiding from exposure to the air oxygen and material is protected from S–O bond formation.

Fig. 2 presents surface morphology and crystalline features of $MnS_2$ and $MnS_2$/CNT thin films. The FE-SEM image (Fig. 2 (b)) of activated CNTs show rough surface of their sidewall, which is caused by oxidation of CNTs by the acidic treatment, however it is not seen in case of pristine CNTs (Fig. 2 (b)). $MnS_2$/CNT thin film (Fig. 2 (c)) shows incorporated $MnS_2$ particles in the porous matrix of CNTs, while $MnS_2$ thin film (Fig. 2 (e)) have porous nanostructure formed with nanoparticles. HR-TEM images (Fig. 2 (e, f)) show that sidewall surface of CNT are non-uniformly attached with few $MnS_2$ nanoparticles. Bright and dark spots are seen in $MnS_2$ nanoparticle (Fig. 2 (f), which increases electroactive sites useful for electrochemical applications. Inset of Fig. 2 (e, f) show selected area electron diffraction (SAED) patterns of CNT and $MnS_2$ nanoparticles, respectively. The SAED pattern of CNTs is indexed with (002), and (100) plane while (002), and (112) planes are indexed for $MnS_2$.

In the literature, promising electrochemical charge storage of manganese is demonstrated in neutral as well as basic electrolytes i.e. $Na_2SO_4$, and KOH, etc [33]. The comparative study of electrochemical charge storage is necessary to decide whether neutral or basic electrolyte is more suitable for $MnS_2$. Hence, as a concept of proof, $MnS_2$, and $MnS_2$/CNT electrodes are analysed in both $Na_2SO_4$ and KOH electrolytes. The CV curves of $MnS_2$ are recorded at different scan rates in 1 M $Na_2SO_4$ (Fig. 3 (a)) and 1 M KOH (Fig. 3 (c)), which show that integrated area of all CV curves of $MnS_2$ are higher in $Na_2SO_4$ electrolyte than KOH. Similarly, occurred in case of $MnS_2$/CNT electrode (Fig. 3 (b, d)). Thus, it is concluded that electrochemical charge storage of $MnS_2$ and its composite with CNT have increased charge storage properties in neutral $Na_2SO_4$ electrolyte than KOH.

Moreover, $MnS_2$/CNT shows more suitable rectangular CV curves and higher integrated area under CV curves in $Na_2SO_4$ as well as in KOH that dictates higher electrochemical charge storage properties of $MnS_2$/CNT electrode over bare $MnS_2$. It is also noted that addition of CNT in $MnS_2$ decreases deep curve of cathodic and anodic peaks for the case of KOH electrolyte, which is attributed to the stabilization of composite ($MnS_2$/CNT) electrode because of CNT addition in comparison with $MnS_2$ electrode. $MnS_2$ and $MnS_2$/CNT electrodes show operating potential window of 0 to +1.0 V/SCE in $Na_2SO_4$ and -0.8 to +0.4 V/SCE in KOH. Positive and negative potential shift is observed during oxidation and reduction of material, respectively with increased scan rate (in case of KOH electrolyte) caused by limitation of ion diffusion rate at higher scan rates [40,41], However, no clear cathodic or anodic peaks are observed in $Na_2SO_4$ indicating that reversible and surface confined electron transfer reactions occur between $Na^+$ and $MnS_2$. The observed CV curves of $MnS_2$/$Na_2SO_4$ are consequences of reversible electron transfer activity between $MnS_2$ and $Na^+$ ions proposed by following equation [33],

$$MnS_2 + Na^+ + e \leftrightarrow MnS_2Na \quad (1)$$

However, in KOH electrolyte, the reversible faradaic reactions between $MnS_2$ and $OH^-$ are occurred for electrochemical charge storage of $MnS_2$ and $MnS_2$/CNT electrodes shown by following equation [42],

$$MnS_2 + OH - \ \leftrightarrow \ - MnS_2OH + e^- \quad (2)$$

For $MnS_2$/CNT electrode, additional redox reactions are occurred due to surface functional groups of activated CNTs proposed by following equations (5)–(7).

$$> C - OOH \leftrightarrow \ - COO + H^+ + e^- \quad (3)$$

$$> C - O + e \leftrightarrow \ > C - O^- \quad (4)$$

$$> C - OH \leftrightarrow \ > C = O + H^+ + e^- \quad (5)$$

The GCD study of $MnS_2$ (Fig. 3 (e, g)) and $MnS_2$/CNT electrodes (Fig. 3 (g, h)) in $Na_2SO_4$ and KOH electrolytes, respectively at different current densities (1–4 mA $cm^{-2}$) show similar results as in CV study. However, all GCD curves of $MnS_2$ and $MnS_2$/CNT electrodes show symmetrical charging and discharging profiles and less initial resistance in the discharging path and longer duration in $Na_2SO_4$ demonstrating more suitability of $MnS_2$ in $Na_2SO_4$ for electrochemical charge storage. Moreover, GCD curves show steeper nature between 0.2 and 0.8 V/SCE potential caused by CNTs addition, which is indicative of double layer charge storage contribution in $MnS_2$/CNT thin film. Initial linear region of discharging curve is associated with redox reactions demonstrated in eqs (5) and (6). The specific capacitances of electrode are calculated for different current densities using following relation,

$$\text{Specific capacitance} = \frac{I_d}{V} \times \frac{t_d}{m} \quad (6)$$

where, $I_d$, $t_d$, $V$, and $m$ correspond to applied current density (mA $cm^{-2}$), discharging time (s), applied potential window (V/SCE), and mass loading of electrode (g). The specific capacitances of $MnS_2$ and $MnS_2$/CNT electrodes are calculated based on discharging time and mass loadings in $Na_2SO_4$ and KOH electrolytes and found that maximum of 855 F $g^{-1}$ specific capacitance is obtained for $MnS_2$/CNT electrodes at 1 mA $cm^{-2}$ current density in 1 M $Na_2SO_4$ (Fig. 3(i)) compared with 669 F $g^{-1}$ in 1 M KOH. Also, comparative study of specific capacitances of $MnS_2$ and $MnS_2$/CNT electrodes show that rate capability of $MnS_2$/CNT electrode is higher in both KOH and $Na_2SO_4$, as compared with bare $MnS_2$ electrode (Fig. 3(i)). This is also observed elsewhere in the

**Table 1**
Comparative $R_s$ and $R_{ct}$ values of $MnS_2$ and $MnS_2$/CNT in $Na_2SO_4$ and KOH electrolytes.

| Sr. no. | Resistance / Electrode - Electrolyte | $MnS_2$–$Na_2SO_4$ | $MnS_2$/CNT- $Na_2SO_4$ | $MnS_2$–KOH | $MnS_2$/CNT- KOH |
|---|---|---|---|---|---|
| 1 | $R_s$ ($\Omega$ $cm^{-2}$) | 2.9 | **0.72** | 1.4 | 1.2 |
| 2 | $R_{ct}$ ($\Omega$ $cm^{-2}$) | 2.4 | **2.1** | 25.6 | 20.8 |

literature owing to addition of CNT in the electrode [43]. Thus CV and GCD studies show that $Na_2SO_4$ is more suitable electrolyte than KOH for $MnS_2$ and it's composite for electrochemical capacitor application. The increase in specific capacitances for $MnS_2$/CNT electrode than $MnS_2$ electrode is associated with short electron transfer due to CNTs and lowest intrinsic resistance of $MnS_2$/CNT electrode in $Na_2SO_4$ (Fig. S4).

The increased electrochemical charge storage of $MnS_2$ in $Na_2SO_4$ is supported by electrochemical impedance analyses within 0.1–$10^5$ Hz frequency range presented in Fig. 3 (j). The impedance study of electrode gives various resistances associated with transfer of electrons from electrolyte ions to electrode matrix. It consists of Warburg resistance (W) associated with transport of ions through electrolyte solution, charge transfer resistance ($R_{ct}$) linked with electron transfer between electrolyte ions and particles in the solid electrode matrix (here $MnS_2$) and equivalent series resistance (ESR) ($R_s$), which is combination of ohmic resistance of wire, current collector, electrode material and electrolyte [37]. Fig. 3 (j) presents comparative impedance profiles of $MnS_2$, and $MnS_2$/CNT electrodes in 1 M $Na_2SO_4$ and 1 M KOH electrolytes.

The initial intersection of impedance profiles in high frequency region show that $MnS_2$/CNT electrode has lowest $R_s$ (0.72 $\Omega$ $cm^{-2}$) and $R_{ct}$ (2.1 $\Omega$ $cm^{-2}$) in $Na_2SO_4$ compared with corresponding values in KOH ($R_s$ = 1.2 $\Omega$ $cm^{-2}$ and $R_{ct}$ = 20.8 $\Omega$ $cm^{-2}$) electrolyte and it is also less than resistances of $MnS_2$ electrode in $Na_2SO_4$ ($R_s$ = 2.9 $\Omega$ $cm^{-2}$, $R_{ct}$ = 2.4 $\Omega$ $cm^{-2}$) and KOH ($R_s$ = 1.4 $\Omega$ $cm^{-2}$, $R_{ct}$ = 25.6 $\Omega$ $cm^{-2}$) (Table 1). Also, small Warburg resistance spike is observed in case of $MnS_2$/CNT in $Na_2SO_4$ comparison with other combinations, indicating higher charge storage properties of $MnS_2$/CNT in $Na_2SO_4$. Thus, lowest ESR and $R_{ct}$ values of $MnS_2$/CNT electrode support to the higher specific capacitance of $MnS_2$/CNT electrode in $Na_2SO_4$ electrolyte as evaluated in CV and GCD studies. It is due to improved charge storage kinetics of $MnS_2$/CNT electrode (demonstrated by schematic representation in Fig. S4) and reduction in ESR, charge transfer resistance and Warburg resistances in $Na_2SO_4$. The electrochemical cyclic life time of $MnS_2$/CNT electrode is evaluated in both KOH and $Na_2SO_4$ for successive 5000 cycles measured at 4 mA $cm^{-2}$ current density (Fig. 3 (l)). It shows higher capacitance retention in $MnS_2$/CNT electrode in $Na_2SO_4$ (90.1%) compared with KOH (86.4%) after cyclic study. The FE-SEM images of $MnS_2$/CNT electrode after cycling process of $MnS_2$/CNT electrode are presented in Fig. S5 that shows maintained surface nanostructure of $MnS_2$/CNT electrode after cycling.

## 4. Conclusions

$MnS_2$ and $MnS_2$/CNT electrodes were prepared on large scale (5 × 10 $cm^2$) with porous nanostructured surface morphologies using dip dry and SILAR methods. The comparative electrochemical charge storage of both the electrodes was assessed in $Na_2SO_4$ and KOH electrolyte systematically using CV, GCD and impedance techniques. $MnS_2$/CNT electrode shown superior electrochemical charge storage in $Na_2SO_4$ with highest 855 F $g^{-1}$ specific capacitance at 1 mA $cm^{-2}$ current density and 90.1% capacitance retention after successive 5000 charge discharge cycles. The highest charge storage properties of $MnS_2$/CNT electrode in $Na_2SO_4$ are associated with improved electron transfer and lowest $R_s$ (0.72 $\Omega$ $cm^{-2}$) value. Thus, current work proposes $Na_2SO_4$ as a more suitable electrolyte for electrochemical capacitor application of $MnS_2$/CNT electrode.

## Credit author statement

Rahul B Pujari: Conceptualization, Methodology, Software, Writing; Abhishek C. Lokhande: Software, Validation; Abhijeet R. Shelke: Visualization, Investigation; Shital B. Kale: Reviewing and Editing; Dong-Weon Lee: Supervision; Chandrakant D. Lokhande: Data curation, Writing – original draft.

## Declaration of competing interest

The authors declare that they have no known competing financial interests or personal relationships that could have appeared to influence the work reported in this paper.

## Acknowledgement

This work was supported by the National Research Foundation of Korea (NRF) grant funded by the Korea government (MSIT) (No. 2020R1A5A8018367).

Authors are thankful to the Department of Science and Technology, Govt. of India for financial support through research project, Materials for Energy Storage, sanction no. [DST/TMD/MES.2K17/04 (C&G)] dated 17th July 2018.

## Appendix A. Supplementary data

Supplementary data to this article can be found online at https://doi.org/10.1016/j.solidstatesciences.2020.106449.

## References

[1] S.L. Zhai, H.E. Karahan, C.J. Wang, Z.X. Pei, L. Wei, Y. Chen, 1D supercapacitors for emerging electronics: current status and future directions, Adv. Mater. 32 (2020).
[2] G.Y. Chen, Y.L. Ai, I.T. Mugaanire, W.J. Ma, B.S. Hsiao, K. Hou, M.F. Zhu, A simple inorganic hybrids strategy for graphene fibers fabrication with excellent electrochemical performance, J. Power Sources (2020) 450.
[3] X. Chen, N.S. Villa, Y.F. Zhuang, L.Z. Chen, T.F. Wang, Z.D. Li, T.T. Kong, Stretchable supercapacitors as emergent energy storage units for health monitoring bioelectronics, Adv Energy Mater 10 (2020).
[4] C.F. Ding, L.B. Huang, X.D. Yan, F. Dunne, S. Hong, J.L. Lan, Y.H. Yu, W.H. Zhong, X.P. Yang, Robust, superelastic hard carbon with in situ ultrafine crystals, Adv. Funct. Mater. 30 (2020).
[5] W.L. Hong, L.Y. Lin, Studying the substrate effects on energy storage abilities of flexible battery supercapacitor hybrids based on nickel cobalt oxide and nickel cobalt oxide@nickel molybdenum oxide, Electrochim. Acta 308 (2019) 83–90.
[6] D. Chen, K. Jiang, T.T. Huang, G.Z. Shen, Recent advances in fiber supercapacitors: materials, device configurations, and applications, Adv. Mater. 32 (2020).
[7] L. Liu, A.R. Liu, Y.H. Xu, F.Q. Yang, J. Wang, Q. Deng, Z.L. Zeng, S.G. Deng, Fabrication of dual-hollow heterostructure of $Ni_2CoS_4$ sphere and nanotubes as advanced electrode for high-performance flexible all-solid-state supercapacitors, J. Colloid Interface Sci. 564 (2020) 313–321.
[8] M.L. Wang, Y.F. Yu, M.Z. Cui, X. Cao, W.F. Liu, C. Wu, X.G. Liu, T.Y. Zhang, Y. Z. Huang, Development of polyoxometalate-anchored 3D hybrid hydrogel for high-performance flexible pseudo-solid-state supercapacitor, Electrochim. Acta 329 (2020).
[9] X.Y. Xu, J.H. Liu, X. Ouyang, L.F. Cui, J.L. Hong, X. Meng, S.Y. Qin, C. Liu, J. N. Tang, D.Z. Chen, In-situ temperature regulation of flexible supercapacitors by

designing intelligent electrode with microencapsulated phase change materials, Electrochim. Acta (2020) 334.
[10] Z. Tian, J.H. Yin, X.M. Wang, Y.Z. Wang, Construction of $Ni_3S_2$ wrapped by rGO on carbon cloth for flexible supercapacitor application, J. Alloys Compd. 777 (2019) 806–811.
[11] Z.Y. Gao, C. Chen, J.L. Chang, L.M. Chen, P.Y. Wang, D.P. Wu, F. Xu, Y.M. Guo, K. Jiang, Enhanced cycleability of faradic $CoNi_2S_4$ electrode by reduced graphene oxide coating for efficient asymmetric supercapacitor, Electrochim. Acta 281 (2018) 394–404.
[12] L. Xu, R.Y. Shi, H.F. Li, C.P. Han, M.Y. Wu, C.P. Wong, F.Y. Kang, B.H. Li, Pseudocapacitive anthraquinone modified with reduced graphene oxide for flexible symmetric all-solid-state supercapacitors, Carbon 127 (2018) 459–468.
[13] S. Ranganatha, N. Munichandraiah, gamma-MnS nanoparticles anchored reduced graphene oxide: electrode materials for high performance supercapacitors, J Sci-Adv Mater Dev 3 (2018) 359–365.
[14] S. Kandula, K.R. Shrestha, N.H. Kim, J.H. Lee, Fabrication of a 3D hierarchical sandwich $Co_9S_8$/alpha-MnS@N-C (R) $MoS_2$ nanowire architectures as advanced electrode material for high performance hybrid supercapacitors, Small 14 (2018).
[15] X.F. Li, J.F. Shen, N. Li, M.X. Ye, Fabrication of γ-MnS/rGO composite by facile one-pot solvothermal approach for supercapacitor applications, J. Power Sources 282 (2015) 194–201.
[16] R.B. Pujari, A.C. Lokhande, A.A. Yadav, J.H. Kim, C.D. Lokhande, Synthesis of MnS microfibers for high performance flexible supercapacitors, Mater. Des. 108 (2016) 510–517.
[17] Y.F. Tang, S.J. Chen, S.C. Mu, T. Chen, Y.Q. Qiao, S.X. Yu, F.N. Gao, Synthesis of capsule-like porous hollow nanonickel cobalt sulfides via cation exchange based on the kirkendall effect for high-performance supercapacitors, Acs Appl Mater Inter 8 (2016) 9721–9732.
[18] J.P. He, C. Guo, S.W. Zhou, Y.L. Zhao, Q.P. Wang, S. Yang, J.Q. Yang, Q.H. Wang, Dual carbon-modified nickel sulfide composites toward high-performance electrodes for supercapacitors, Inorg Chem Front 6 (2019) 226–232.
[19] Q. Hu, X.F. Zou, Y.H. Huang, Y.Q. Wei, YaWang, F. Chen, B. Xiang, Q.B. Wu, W. P. Li, Graphene oxide-drove transformation of NiS/$Ni_3S_4$ microbars towards $Ni_3S_4$ polyhedrons for supercapacitor, J. Colloid Interface Sci. 559 (2020) 115–123.
[20] X.B. Xu, W. Zhong, X. Zhang, J. Dou, Z.G. Xiong, Y. Sun, T.T. Wang, Y.W. Du, Flexible symmetric supercapacitor with ultrahigh energy density based on NiS/$MoS_2$@N-rGO hybrids electrode, J. Colloid Interface Sci. 543 (2019) 147–155.
[21] R. Zhang, C.X. Lu, Z.L. Shi, T. Liu, T.F. Zhai, W. Zhou, Hexagonal phase NiS octahedrons co-modified by 0D-, 1D-, and 2D carbon materials for high-performance supercapacitor, Electrochim. Acta 311 (2019) 83–91.
[22] Y.X. Cui, J. Zhang, G.Y. Li, Y. Sun, G.F. Zhang, W.J. Zheng, Ionic liquid-assisted synthesis of rGO wrapped three-dimensional CuS ordered nanoerythrocytes with enhanced performance for asymmetric supercapacitors, Chem. Eng. J. 325 (2017) 424–432.
[23] W.B. Li, W.M. Song, H.H. Wang, Y.M.O. Kang, In situ self-assembly of $Ni_3S_2$/MnS/CuS/reduced graphene composite on nickel foam for high power supercapacitors, RSC Adv. 9 (2019) 31532–31542.
[24] W. Xiao, W.J. Zhou, T. Feng, Y.H. Zhang, H.D. Liu, H. Yu, L.L. Tian, Y. Pu, One-pot solvothermal synthesis of flower-like copper sulfide/reduced graphene oxide composite superstructures as high-performance supercapacitor electrode materials, J. Mater. Sci. Mater. Electron. 28 (2017) 5931–5940.
[25] M. Yang, J. Choi, S.K. Kim, P.V. Braun, Flexible binder-free CuS/Polydopamine-Coated carbon cloth for high voltage supercapacitors, Energy Technol-Ger 6 (2018) 1852–1858.
[26] S. Ramki, K. Pandi, S.-M. Chen, Y.-T. Ye, T.-W. Chen, Q. Hao, Hydrothermal synthesis of manganese sulfide decorated graphene oxide for effective electrochemical sensing of dopamine, Int. J Electrochem Sci 14 (2019) 1069–1081.
[27] Y.I. Liu, L.P. Li, J.H. Zhu, T. Meng, L. Ma, H. Zhang, M.W. Xu, J. Jiang, C.M. Li, One-Dimensional integrated MnS@carbon nanoreactors hybrid: an alternative anode for full-cell Li-ion and Na-ion batteries, Acs Appl Mater Inter 10 (2018) 27911–27919.
[28] J.L. Xu, L. Zhang, G.C. Xu, Z.P. Sun, C. Zhang, X. Ma, C.L. Qi, L. Zhang, D.Z. Jia, Facile synthesis of NiS anchored carbon nanofibers for high-performance supercapacitors, Appl. Surf. Sci. 434 (2018) 112–119.
[29] Y. Yang, M.L. Li, J.N. Lin, M.Y. Zou, S.T. Gu, X.J. Hong, L.P. Si, Y.P. Cai, MOF-derived $Ni_3S_4$ encapsulated in 3D conductive network for high-performance supercapacitor, Inorg. Chem. 59 (2020) 2406–2412.
[30] N.R. Chodankar, I.V. Bagal, S.-W. Ryu, D.-H. Kim, Hybrid material passivation approach to stabilize the silicon nanowires in aqueous electrolyte for high-energy efficient supercapacitor, Chem. Eng. J. 362 (2019) 609–618.
[31] X. Yu, C. Li-yun, H. Jian-feng, L. Jia, F. Jie, Y. Chun-yan, Influence of S/Mn molar ratio on the morphology and optical property of γ-MnS thin films prepared by microwave hydrothermal, J. Alloys Compd. 549 (2013) 1–5.
[32] R.B. Pujari, G.S. Gund, S.J. Patil, H.S. Park, D.-W. Lee, Anion-exchange phase control of manganese sulfide for oxygen evolution reaction, J. Mater. Chem. 8 (2020) 3901–3909.
[33] R. Pujari, V. Lokhande, U. Patil, D. Lee, C. Lokhande, Controlled sulfurization of $MnCO_3$ microcubes architectured $MnS_2$ nanoparticles with 1.7 fold capacitance increment for high energy density supercapacitor, Electrochim. Acta 301 (2019) 366–376.
[34] M.M. Huq, C.-T. Hsieh, C.-Y. Ho, Preparation of carbon nanotube-activated carbon hybrid electrodes by electrophoretic deposition for supercapacitor applications, Diam. Relat. Mater. 62 (2016) 58–64.
[35] T.K. Pani, B.B. Sahoo, B. Sundaray, Carbon electrodes derived from polyacrylonitrile-polyethylene glycol blend for high-performance supercapcitor, Mater. Res. Express 6 (2019).
[36] W. Cui, Q. Liu, N.Y. Cheng, A.M. Asiri, X.P. Sun, Activated carbon nanotubes: a highly-active metal-free electrocatalyst for hydrogen evolution reaction, Chem. Commun. 50 (2014) 9340–9342.
[37] R. Pujari, A. Lokhande, J. Kim, C. Lokhande, Bath temperature controlled phase stability of hierarchical nanoflakes CoS 2 thin films for supercapacitor application, RSC Adv. 6 (2016) 40593–40601.
[38] S. Liu, C. Mao, Y. Niu, F. Yi, J. Hou, S. Lu, J. Jiang, M. Xu, C. Li, Facile synthesis of novel networked ultralong cobalt sulfide nanotubes and its application in supercapacitors, Acs Appl Mater Inter 7 (2015) 25568–25573.
[39] P. Jagadish, M. Khalid, N. Amin, M.T. Hajibeigy, L.P. Li, A. Numan, N.M. Mubarak, R. Walvekar, A. Chan, Recycled carbon fibre/$Bi_2Te_3$ and $Bi_2S_3$ hybrid composite doped with MWCNTs for thermoelectric applications, Composites, Part B 175 (2019) 107085.
[40] R. Pujari, A. Lokhande, A. Shelke, J. Kim, C. Lokhande, Chemically deposited nano grain composed $MoS_2$ thin films for supercapacitor application, J. Colloid Interface Sci. 496 (2017) 1–7.
[41] T. Sun, Z. Li, X. Liu, L. Ma, J. Wang, S. Yang, Facile construction of 3D graphene/$MoS_2$ composites as advanced electrode materials for supercapacitors, J. Power Sources 331 (2016) 180–188.
[42] X. Li, J. Shen, N. Li, M. Ye, Fabrication of γ-MnS/rGO composite by facile one-pot solvothermal approach for supercapacitor applications, J. Power Sources 282 (2015) 194–201.
[43] D.P. Dubal, G.S. Gund, C.D. Lokhande, R. Holze, Decoration of spongelike $Ni(OH)_2$ nanoparticles onto MWCNTs using an easily manipulated chemical protocol for supercapacitors, Acs Appl Mater Inter 5 (2013) 2446–2454.